

Storm Time Electrified MSTIDs Observed over Mid-Latitude North America

Ian James Kelley¹, Bharat Simha Reddy Kunduri¹, J. B. H. Baker¹, John Michael Ruohoniemi¹, and Simon George Shepherd²

¹Virginia Tech

²Dartmouth College

November 21, 2022

Abstract

Medium-scale Traveling Ionospheric Disturbances (MSTIDs) are prominent and ubiquitous features of the mid-latitude ionosphere, and are observed in Super Dual Auroral Radar Network (SuperDARN) and high-resolution Global Navigational Satellite Service (GNSS) Total Electron Content (TEC) data. The mechanisms driving these MSTIDs are an open area of research, especially during geomagnetic storms. Previous studies have demonstrated that night-side MSTIDs are associated with an electrodynamic instability mechanism like Perkins, especially during geomagnetically quiet conditions. However, day-side MSTIDs are often associated with atmospheric gravity waves. Very few studies have analyzed the mechanisms driving MSTIDs during strong geomagnetic storms at mid-latitudes. In this study, we present mid-latitude MSTIDs observed in de-trended GNSS TEC data and SuperDARN radars over the North American sector, during a geomagnetic storm (peak Kp reaching 9) on September 7-8, 2017. In SuperDARN, MSTIDs were observed in ionospheric backscatter with Line Of Sight (LOS) velocities exceeding 800 m/s. Additionally, radar LOS velocities oscillated with amplitudes reaching ± 500 m/s as the MSTIDs passed through the fields-of-view. In detrended TEC, these MSTIDs produced perturbations reaching ~ 50 percent of background TEC magnitude. The MSTIDs were observed to propagate in the westward/south-westward direction with a time period of ~ 15 minutes. Projecting de-trended GNSS TEC data along SuperDARN beams showed that enhancements in TEC were correlated with enhancements in SuperDARN SNR and positive LOS velocities. Finally, SuperDARN LOS velocities systematically switched polarities between the crests and the troughs of the MSTIDs, indicating the presence of polarization electric fields and an electrodynamic instability process during these MSTIDs.

1 **Storm Time Electrified MSTIDs Observed over**
2 **Mid-Latitude North America**

3 **I. J. Kelley ¹, B. S. R. Kunduri¹, J. B. H. Baker ¹, J. M. Ruohoniemi ¹, S. G.**
4 **Shepherd ²**

5 ¹Bradley Department of Electrical and Computer Engineering, Virginia Tech, Blacksburg, Virginia, USA.
6 ²Thayer School of Engineering, Dartmouth College, Hanover, NH, USA

7 **Key Points:**

- 8 • MSTID signatures were observed in GNSS TEC and SuperDARN ionospheric backscat-
9 ter during a strong geomagnetic storm.
10 • MSTID characteristics were broadly consistent between the datasets, with peri-
11 ods of 10-20 min and phase speeds of ~ 800 m/s.
12 • SuperDARN LOS velocities systematically switched polarities between MSTID
13 crests and troughs, indicating polarization electric fields.

Corresponding author: I. J. Kelley, ikelley@vt.edu

Abstract

Medium-scale Traveling Ionospheric Disturbances (MSTIDs) are prominent and ubiquitous features of the mid-latitude ionosphere, and are observed in Super Dual Auroral Radar Network (SuperDARN) and high-resolution Global Navigational Satellite Service (GNSS) Total Electron Content (TEC) data. The mechanisms driving these MSTIDs are an open area of research, especially during geomagnetic storms. Previous studies have demonstrated that night-side MSTIDs are associated with an electrodynamic instability mechanism like Perkins, especially during geomagnetically quiet conditions. However, day-side MSTIDs are often associated with atmospheric gravity waves. Very few studies have analyzed the mechanisms driving MSTIDs during strong geomagnetic storms at mid-latitudes. In this study, we present mid-latitude MSTIDs observed in de-trended GNSS TEC data and SuperDARN radars over the North American sector, during a geomagnetic storm (peak K_p reaching 9) on September 7-8, 2017. In SuperDARN, MSTIDs were observed in ionospheric backscatter with Line Of Sight (LOS) velocities exceeding 800 m/s. Additionally, radar LOS velocities oscillated with amplitudes reaching ± 500 m/s as the MSTIDs passed through the fields-of-view. In detrended TEC, these MSTIDs produced perturbations reaching ~ 50 percent of background TEC magnitude. The MSTIDs were observed to propagate in the westward/south-westward direction with a time period of ~ 15 minutes. Projecting de-trended GNSS TEC data along SuperDARN beams showed that enhancements in TEC were correlated with enhancements in SuperDARN SNR and positive LOS velocities. Finally, SuperDARN LOS velocities systematically switched polarities between the crests and the troughs of the MSTIDs, indicating the presence of polarization electric fields and an electrodynamic instability process during these MSTIDs.

1 Introduction

Traveling Ionospheric Disturbances (TIDs) (Munro, 1948) are wave-like structures which propagate through the ionosphere. TIDs are most commonly expected to be driven by Atmospheric Gravity Waves (AGWs) originating in the neutral atmosphere (Hines, 1960) and can be sensed with instruments used for monitoring ionospheric dynamics such as Global Navigational Satellite Service (GNSS) Total Electron Content (TEC) (Saito et al., 1998) and coherent scatter radars (Samson et al., 1990; Fukao et al., 1991). TIDs are further classified as either Large-Scale (LSTIDs) or MSTIDs based on their spatio-temporal scales (Georges, 1968). MSTIDs typically have a time-period of 15-60 minutes, phase velocities of 100-300 m/s, and wavelengths between 200-800km. On the other hand LSTIDs have phase speeds between 400-1000 m/s, periods above 30 minutes, and wavelengths above 1000 km (Hocke & Schlegel, 1996; Hunsucker, 1982). The differences between MSTIDs and LSTIDs are not just limited to their spatio-temporal scales, previous studies have shown that the underlying generation mechanisms and the physics of their propagation also differ (Hocke & Schlegel, 1996). MSTIDs are often linked to Atmospheric Gravity Waves (AGWs), which are a neutral atmospheric phenomenon generally carrying more energy than the TIDs themselves (Hunsucker, 1982). Such AGW-driven MSTIDs are more commonly reported at high latitudes, and on the day-side, and in the winter (Bristow et al., 1994; Frissell et al., 2014). The AGWs are in turn expected to be driven by factors such tropospheric weather (Chou et al., 2017), Joule heating (Chimonas & Hines, 1970), and ground-based disturbances including tsunamis and earthquakes (Liu et al., 2011). Determining the sources of AGWs/MSTIDs can be challenging since they travel thousands of kilometers from the source and dissipate along the propagation paths (e.g., Vadas, 2007; Ogawa et al., 2009). Previous studies have demonstrated the utility of SuperDARN for analyzing MSTIDs (e.g., Samson et al., 1990; Bristow et al., 1994; Grocott et al., 2013; Frissell et al., 2014). In particular, these studies have shown that quasiperiodic density rarefactions and enhancements in ionospheric layers produced by MSTIDs manifest as moving bands of enhanced ground scatter power in SuperDARN observations.

66 In addition to AGWs, MSTIDs have also been associated with electrodynamic instabilities (Perkins, 1973; Miller, 1997). Such MSTIDs are linked to perturbations and oscillations in electric fields (e.g., Shiokawa et al., 2003; Otsuka et al., 2004, 2007; Suzuki et al., 2009). A few studies showed that these electrodynamic instabilities can map into the other hemisphere along magnetic field lines and drive MSTIDs in the conjugate location (Otsuka et al., 2004; Valladares & Sheehan, 2016). Electrified MSTIDs exhibit properties that are different from those linked to AGWs. Specifically, electrified MSTIDs were frequently observed on the night-side, propagating southwestwards. A majority of previous studies have reported electrified MSTIDs during quiet geomagnetic conditions and in summer months (Ogawa et al., 2009; Duly et al., 2013; Huang et al., 2016). Electrified MSTIDs are an active area of research and the mechanisms seeding the instability processes are yet to be fully understood. For example, it has been shown that the growth rate of the instability alone is not sufficient to seed nighttime MSTIDs (Garcia et al., 2000), and coupling with the E-region and sporadic-E instabilities can re-inforce the process (Otsuka et al., 2007; Ogawa et al., 2009). A few previous studies have used measurements from airglow imagers or TEC in combination with SuperDARN observations of electric fields to analyze the behavior and characteristics of electrified MSTIDs during geomagnetically quiet conditions (e.g., Ogawa et al., 2009; Suzuki et al., 2009). Two main features were reported by these studies. First, the Doppler Line of Sight (LOS) velocities switched polarities as the crests and troughs associated with the MSTIDs passed through the radar’s field-of-view. Secondly, depletions in airglow intensity and TEC were correlated with enhancements in SuperDARN ionospheric backscatter power.

68 Geomagnetic storms have often been shown to drive significant LSTID activity (e.g. Ding et al., 2007; Borries et al., 2009). However, very few studies have reported and analyzed storm-time MSTIDs (e.g., S. R. Zhang et al., 2019). Such disturbed intervals can be challenging to analyze since several different factors such as neutral winds, Sub-Auroral Polarization Streams (SAPS), and strong ion-neutral coupling can be active simultaneously (Guo et al., 2018; S. R. Zhang et al., 2019), especially at mid-latitudes. For example, Guo et al. (2018) suggested that thermospheric heating by SAPS electric fields can induce regional disturbances which manifest as AGWs and TIDs. In addition, changes in neutral winds induced by SAPS electric fields (e.g., S. Zhang et al., 2017) can drive changes in the propagation of AGWs and associated TIDs. While Joule heating during geomagnetic storms is expected to drive AGWs and TIDs, a few studies have hypothesized the possibility that electrodynamic instabilities can also play a role (S. R. Zhang et al., 2019). Overall, there has been very limited focus on analyzing the role of electrodynamic instabilities in driving MSTIDs during geomagnetic storms.

102 In this study, US mid-latitude SuperDARN observations are used alongside high-resolution GNSS TEC data to analyze MSTID activity during a strong geomagnetic storm that took place on Sep 7-8, 2017. The MSTID characteristics (wavelength, time period, etc) are derived from these two datasets and compared. We determine that the MSTID activity in this event was associated with an electrodynamic instability.

107 2 Datasets

108 The Fort Hays, Kansas, and Christmas Valley, Oregon, mid-latitude SuperDARN radars are used to study the MSTIDs observed during this event. High-resolution GNSS TEC in the North American sector is used in conjunction with SuperDARN to characterize the MSTIDs. In this section, these datasets will be defined. Their coverage, techniques, and data will be outlined in the following section. Additionally, datasets used for capturing geomagnetic indices will be defined.

114

2.1 SuperDARN

115

116

117

118

119

120

121

122

123

124

125

126

127

128

129

SuperDARN is a global network of High-Frequency (HF) radars covering polar, high, and mid-latitudes in the Northern and Southern Hemispheres (Greenwald et al., 1995; Chisham et al., 2007; Nishitani et al., 2019). SuperDARN radars observe coherent backscatter from decameter-scale irregularities aligned along the geomagnetic field. The Doppler velocity of the back-scattered signal is proportional to the LOS component of $E \times B$ plasma drift within the scattering region (Ruohoniemi et al., 1987). The radars electronically steer across different look directions. A radar typically scans through 16 beams in 1 minute, covering $\sim 50^\circ$ of azimuth. The first SuperDARN radar came into operation at Goose Bay, Labrador (Canada) in 1983. Over the following decades many others were built to improve coverage across the high-latitude regions of both the Northern and Southern Hemispheres. The SuperDARN network later expanded to the mid-latitudes to enable observations of plasma convection during intervals of very strong geomagnetic activity when the auroral oval and convection extend equatorwards (Baker et al., 2007; Nishitani et al., 2019). The most commonly used SuperDARN parameters include power which is measured in dB of SNR above the noise floor, and LOS Doppler velocities.

130

2.2 GNSS Total Electron Content

131

132

133

134

135

136

137

138

139

140

141

142

143

144

145

146

147

148

149

150

151

152

Total Electron Content (TEC) is a columnar electron density measurement between a satellite and ground-based receiver. Using Global Navigational Satellite Service (GNSS) constellations allows for widespread TEC measurements across the globe. TEC is typically measured in TEC units (TECU), where $1 \text{ TECU} = 10^{16} \text{ electrons/m}^2$. Worldwide GNSS TEC data is collected and processed at the MIT Haystack Observatory and available from the Madrigal database (<http://www.openmadrigal.org>) (Rideout & Coster, 2006; Vierinen et al., 2016). Several previous studies have shown the utility of GNSS TEC data for monitoring and analyzing MSTIDs over large geographical regions (e.g., Tsugawa et al., 2007; S. R. Zhang et al., 2017, 2019). Data is available at 30 second time cadence, which is more than sufficient for observing MSTID activity (Saito et al., 1998). Each LOS GNSS TEC data point contains satellite, receiver, latitude, longitude, elevation angle, and timestamp, along with the TEC value. Both the American GPS constellation and Russian GLONASS constellation are sources of data in this study. All data points with low elevation angles ($< 30^\circ$ between ray-path and horizon) have been discarded to increase confidence in the measurements. Additionally, vertical TEC values were derived by accounting for the elevation angles. The TEC data from each satellite-receiver pair is de-trended by subtracting a rolling average over a 30-minute sliding window. This approach is similar to the methods discussed in S. R. Zhang et al. (2017) and Lyons et al. (2019), and preferentially selects TIDs with periods less than 30 minutes. High frequency components/noise were not filtered out in this approach. MSTIDs during this event were large in amplitude and prominent, so TEC data processing is not as consequential as compared to geomagnetically quiet intervals when perturbations in TEC are smaller.

153

2.3 Solar wind, IMF and geomagnetic indices

154

155

156

157

158

159

160

In the current study, 1-min averaged OMNI values (King & Papitashvili, 2005), time shifted to the bow shock sub-solar point were used to examine the Interplanetary Magnetic Field (IMF) and solar wind conditions. The impact of geomagnetic disturbances on mid-latitudes electrodynamics were examined using the asymmetric (Asym-H) and symmetric (Sym-H) disturbance indices (Iyemori, 1990). Note that the Sym-H and Asym-H indices have a temporal resolution of 1-minute. Finally, the impact of auroral electrojets during the event was analyzed using the AL and AU indices (Davis & Sugiura, 1966).

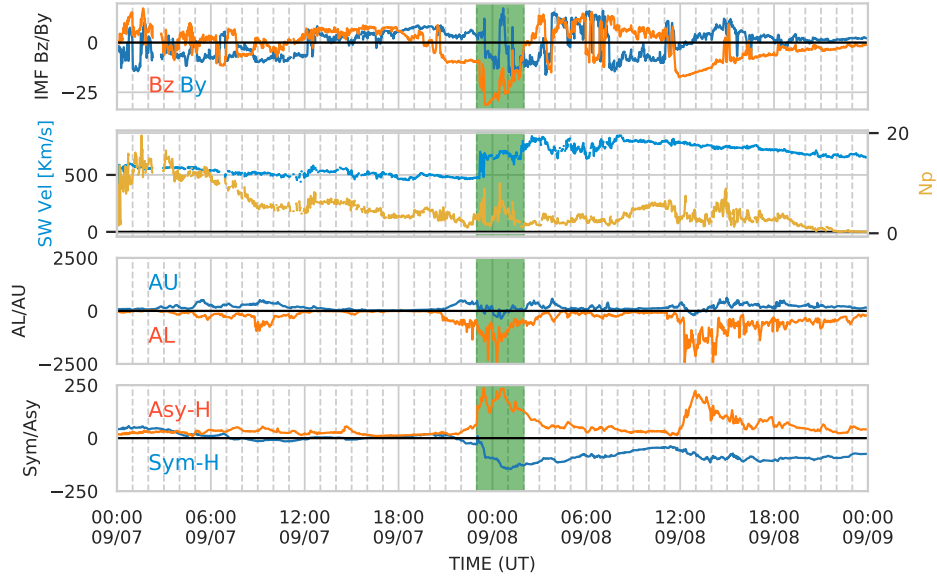


Figure 1. An overview of the geomagnetic conditions on September 7th and 8th, 2017. The conditions are shown over a 48 hour window, with the relevant time period for this study highlighted in green. The top two panels show IMF Bz/By, solar wind speed and density from the OMNI dataset. Third panel shows the auroral electrojet indices AU and AL, and the fourth panel shows the Sym-H/Asy-H indices.

3 Results

3.1 Event Overview

The event analyzed in this study occurred during the main phase of a major geomagnetic storm on Sep 7-8, 2017. Kp reached a peak of 9 at $\sim 1:30$ UT on September 8th, 2017. An overview of the geomagnetic conditions over a 48-hour interval is presented in Figure 1. From top to bottom, the figure presents IMF Bz and By components, solar wind velocity (V_x) and number density, AL and AU indices, and Sym-H and Asy-H indices. The specific period of interest for this study is highlighted in the figure as the time interval between 23 UT on Sep 7, 2017 and 2 UT on Sep 8, 2017. It can be noted that IMF Bz turns sharply negative at $\sim 23:00$ UT on the 7th, dropping to ~ -30 nT by 0:00 UT on the 8th. Around the same time, solar wind velocity increases from km/s to 700 km/s along with multiple upturns in number density. We note that the Sym-H index drops to ~ -200 nT during the interval of interest, marking the main phase of the geomagnetic storm. Finally, elevated AL magnitude (~ -2500 nT) and upticks in the Asy-H index (reaching 250 nT) are indicative of strong substorm activity and enhancement of the partial ring current. Overall, MSTIDs analyzed in this study occurred during an interval of strong geomagnetic driving when SAPS is expected to dominate the sub-auroral ionosphere with velocities reaching several hundred m/s (Kunduri et al., 2018; S. R. Zhang et al., 2019).

3.2 GNSS TEC Observations

A snapshot of raw and de-trended GNSS TEC measurements during the main phase of the storm at 0 UT on Sep 8, 2017 is presented in Figure 2. The top panel of the figure shows raw TEC measurements over the North American continent and the bottom

184 panel show the 30-minute de-trended TEC, scaled according to the color bar on the right.
 185 The outlines of Christmas Valley East beam 18, Fort Hays West beam 18, and Fort Hays
 186 East beam 14 are overlaid in the top-panel to provide context when comparing TEC mea-
 187 surements with SuperDARN in later sections. The de-trended TEC data shows a com-
 188 plex TID pattern including both LSTIDs and MSTIDs. The focus of this study is the
 189 MSTID activity observed in the north-central United States, centered around 45°N , 95°W
 190 (see region outlined in Figure 2.b). For reference, this location is about 150km west of
 191 Minneapolis, Minnesota. An important feature is that the MSTIDs are collocated with
 192 a trough-like feature observed in raw TEC data. A previous study (S. R. Zhang et al.,
 193 2019) reported observations of SAPS by the Millstone Hill ISR during the event, sug-
 194 gesting these MSTIDs could be linked to SAPS flows. The MSTID phase fronts are ori-
 195 ented North-Northwest to South-Southeast, suggesting that the direction of propagation
 196 is West-Southwest.

197 The propagation direction is shown in Figure 3 which displays de-trended TEC as
 198 a function of latitude vs UT (top panel) and longitude vs UT (bottom panel). This fig-
 199 ure considers the de-trended TEC sampled geographically within the region of between
 200 $43\text{-}47^{\circ}\text{N}$ and $108\text{-}112^{\circ}\text{W}$. As the sampled region is small relative to the MSTID struc-
 201 tures, the latitude and longitude plots appear similar. The sampled region for Figure 3
 202 is in the Western portion of the red highlighted area in Figure 2. The perturbations
 203 in de-trended TEC are particularly strong, reaching an amplitude of ± 4 TECu which
 204 forms a significant proportion of the background TEC, which varies between 10-20 TECu.
 205 In Figure 3.a, a slight equator-wards component can be detected. The Westwards ve-
 206 locity component (~ 1 degree per minute) is stronger than the Southward component.
 207 The period of the MSTIDs are consistent between both plots. This period varies from
 208 $\sim 7\text{-}20$ minutes throughout the interval from 0 UT to 2 UT. In the next sections, the per-
 209 turbations in de-trended TEC will be compared with SuperDARN observations and the
 210 role of different factors such as electric fields in driving these MSTIDs will be analyzed.

211 3.3 SuperDARN Observations

212 The US mid-latitude SuperDARN radars were making measurements over the North
 213 American sector during the event. Of particular interest are the Christmas Valley East
 214 (CVE), Christmas Valley West (CVW), Fort Hays East (FHE), and Fort Hays West (FHW)
 215 radars. Fields-of-view of these radars cover the region where MSTIDs were observed in
 216 GNSS TEC. A snapshot of the measurements from the FHE and FHW radars at 0 UT
 217 on Sep 8, 2017 (same time presented in Figure 2) is shown in Figure 4. The top panel
 218 shows the LOS velocities observed by the radars and the bottom panel shows the power,
 219 scaled according to the color bar on the right. The red outline in the bottom panel marks
 220 the same region outlined in Figure 2 where MSTID activity was observed. We can note
 221 that SuperDARN backscatter power exhibits zonal variability, alternating between high
 222 and low-powered regions. It can also be noted that the radars were observing ionospheric
 223 backscatter with LOS speeds reaching 1 km/s. Another feature that stands out is the
 224 systematic transition from positive LOS velocities (blue colored) in FHE to negative LOS
 225 velocities (red colored) in FHW. This behavior suggests that the background plasma con-
 226 vection in the region is predominantly westwards. Multiple US mid-latitude SuperDARN
 227 radars observed strong ionospheric backscatter with LOS speeds reaching 1 km/s in the
 228 region where MSTIDs were observed in GNSS TEC data.

229 3.4 Comparison Between SuperDARN and GNSS TEC Observations

230 Projecting high-resolution GNSS TEC data along SuperDARN beams allows for
 231 direct comparison of the spatio-temporal variability observed in both datasets. GNSS
 232 TEC data is assumed to be sourced from a single pierce-point, which can be mapped within
 233 a given radar beam's footprint, with associated slant range and time. Note that the slant
 234 range for GNSS TEC is not limited to 45km bins as would be the case for SuperDARN

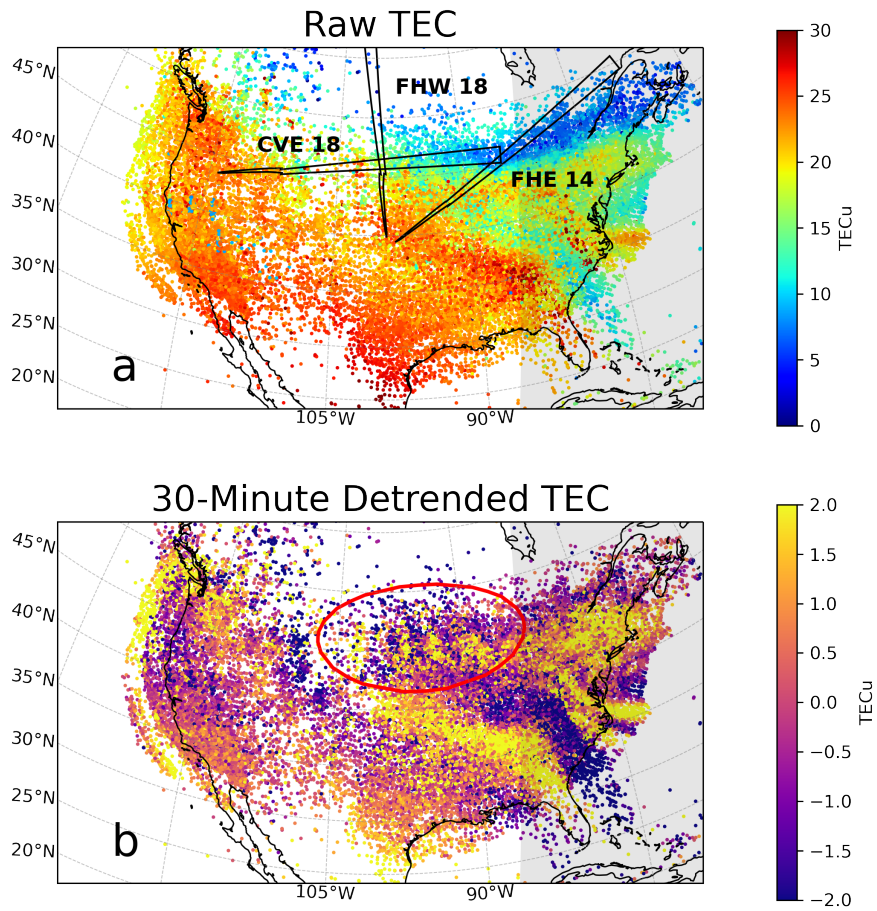


Figure 2. GNSS TEC observations over the North American sector on Sep 8, 2017 at 0:00 UT. Panel (a) shows raw TEC measurements. The outlines of Christmas Valley East radar beam 18, Fort Hays West radar beam 18, and Fort Hays East radar beam 14 are also overlaid on the map. Panel (b) shows 30-minute detrended TEC and the red outline indicates the region of interest with clear MSTID signatures. The grey shaded region denotes the day-night terminator.

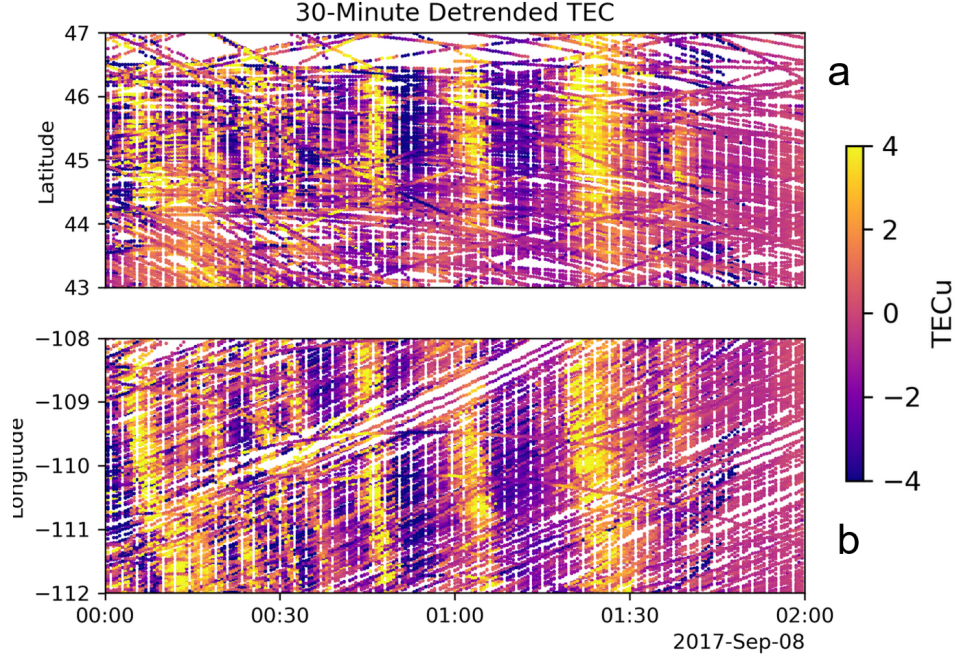


Figure 3. Spatio-temporal variability from TEC sampled with a limited 4x4 degree area. (a) shows de-trended TEC plotted as a function of latitude and UT plot and (b) shows de-trended TEC as a function of longitude and UT. TEC data for this plot is taken between 43-47°N and 108-112°W which corresponds to approximately 800km in slant range on Christmas Valley East beam 18.

235 data, and instead can be considered a continuous measurement. Similarly, the high-resolution
 236 GNSS TEC data has a 30 second time cadence, which is twice as fast as SuperDARN
 237 data which takes 1-2 minutes to complete a full scan across all beams. Despite the dif-
 238 ferences in the spatial and temporal resolutions of these datasets, this technique enables
 239 a direct comparison between observations made by a specific radar beam and the GNSS
 240 TEC within that beam. Figure 5 demonstrates a comparison along beam 18 of the CVE
 241 radar (left most beam marked Figure 2.a). Panel (a) of the figure presents de-trended
 242 TEC data projected along the beam, panel (b) presents the backscatter power observed
 243 on the beam, and panel (c) shows both the overlaid on top of each other. Similar to the
 244 observations presented in Figure 2 strong perturbations can be clearly noted from panel
 245 (a) starting ~2330 UT on Sep 7 and continuing until 2 UT on Sep 8. A very similar “stri-
 246 ation” in SuperDARN power can be observed in panel (b) with enhancements in backscat-
 247 ter power reaching 40 dB. Another interesting feature is that the “striations” can be ob-
 248 served at both near (< 500 km) and far ranges (1000-1500 km), over a total span of al-
 249 most 2000 km. Finally, panel (c) qualitatively shows that the positive perturbations (en-
 250 hancements) in de-trended TEC align well with the enhancements in SuperDARN power.
 251 The relation between de-trended TEC and SuperDARN backscatter power is further in-
 252 vestigated using a correlation analysis in Figure 6 which shows a time-series plot com-
 253 paring de-trended TEC and SuperDARN power between 300-600 km and 0045 and 0200
 254 UT (marked in Figure 5). This range-time interval is chosen because of the absence of
 255 data gaps in both datasets. In this period, peaks in SuperDARN power align well the
 256 peaks in de-trended TEC, especially between 0100 and 0130 UT. A direct correlation be-
 257 tween the two datasets is difficult due to the differences in temporal resolutions between
 258 them and moreover, TECu is a linear unit whereas dB (SuperDARN power) is logarith-
 259 mic. The 1D Pearson correlation coefficient calculated using a two minute rolling aver-

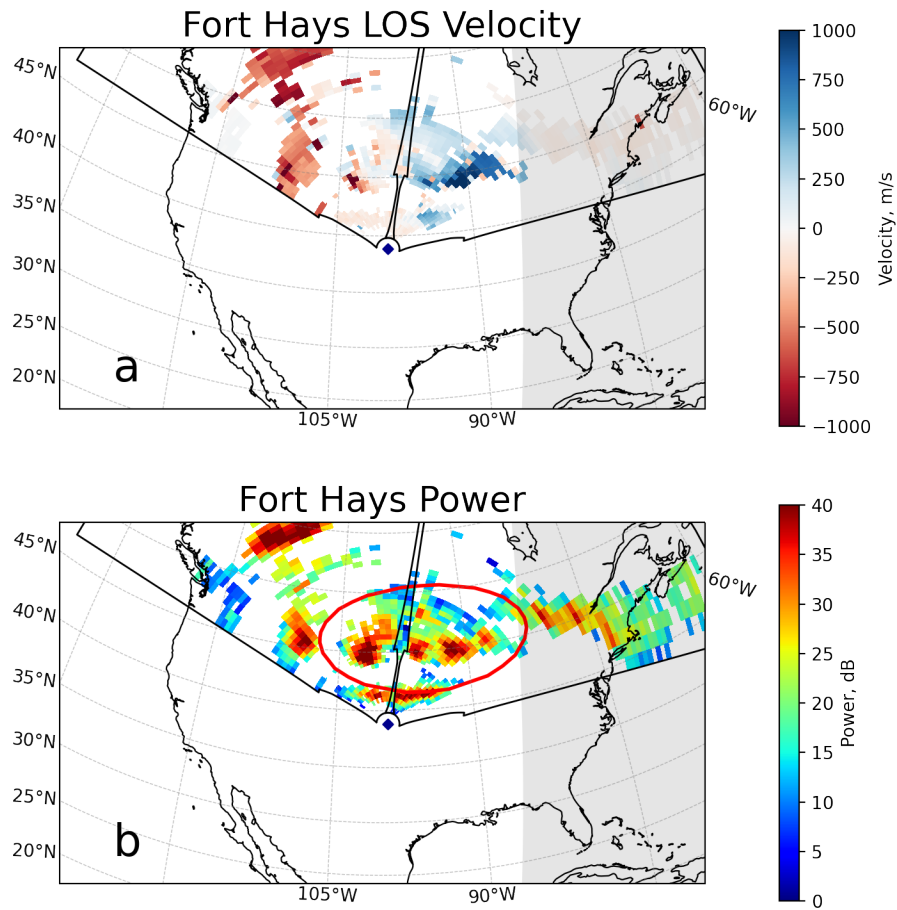


Figure 4. FHE and FHW radar measurements at 0:00UT on September 8th, 2017 (same time as Figure 2). Panel (a) presents SuperDARN LOS velocities scaled according to the color bar on the right. Panel (b) shows the SuperDARN backscatter power. The grey shaded region indicates the day-night terminator.

Table 1. MSTID Characteristics as Determined by SuperDARN and TEC

Characteristic	Value from SuperDARN (CVE 18)	Value from TEC
<i>Wavelength</i>	600 – 800 <i>km</i>	660 <i>km</i>
<i>Phase Speed</i>	800 – 900 <i>m/s</i>	800 <i>m/s</i>
<i>Period</i>	10 – 20 <i>min</i>	10 – 20 <i>min</i>

age over both the datasets was 0.29. The two datasets didn't exhibit a strong correlation, and the differences in the spatio-temporal cadence between the two datasets likely contributed to it. However, it can be qualitatively stated that the peaks in de-trended TEC aligned with enhancements in SuperDARN power. Additionally, an artifact of beam forming SuperDARN radars is that the farther beams off boresight will have non-constant azimuthal angles as elevation increases. This is known as the beam cone, and is described by (André et al., 1998). This means that it is possible that measurements by CVE beam 18 and FHE beam 18 specifically may be slightly shifted from their reported position. However, the scale sizes of the MSTIDs are larger than any potential shift due to the beam cone effect, and it will not have a significant impact on our results.

In Table 1, the characteristics of the MSTIDs estimated from both the datasets are summarized. Specifically, the wavelength, phase speed, and the time-period of the MSTIDs are presented. These values were estimated manually. MSTID period was estimated by calculating the time-interval between two phase fronts, while the phase speed was estimated by calculating the slope of the striations. The process is illustrated in Figure 5.b, where phase fronts are indicated by black lines. Beams that have a more zonal look direction are more suitable for this analysis (such as CVE beam 18 shown in the figure), since they are oriented more along the MSTID propagation direction. Note that the phase speed is different from the LOS velocities measured by SuperDARN radar. Values from SuperDARN radars show wavelengths between 500 and 1000 km, phase speeds of 800-900 m/s (LOS), and a time-period of 10-20 minutes. TEC estimates of these characteristics are in agreement. Estimates vary significantly through the event interval, as differing wave structures appear at different times. TEC estimates were made using Range-Time-Intensity (RTI) TEC plots (Figure 5), and keogram plots (Figure 3). Overall, despite the differences in spatio-temporal coverage between these two datasets, the characteristics of the MSTIDs estimated from them are largely consistent.

So far, the spatio-temporal variations in de-trended TEC and SuperDARN power have been compared and it was demonstrated that enhancements in TEC were collocated with enhancements in SuperDARN power. In Figure 7, a comparison between de-trended TEC and SuperDARN LOS vectors is presented along beam 14 of the FHE radar. In a format similar to Figure 5, panel (a) presents de-trended TEC, panel (b) shows LOS velocities along FHE beam 14, and panel (c) shows both the datasets overlaid on top of each other. Similar to the observations presented in Figure 5, strong perturbations in TEC can also be observed along this beam. Note that the color bar for SuperDARN LOS velocities shown in panel (b) is centered on 150 m/s to bring out the oscillations in velocities. It can be seen that the LOS velocities between 2330 UT and 0100 UT and 300-1200 km range oscillate around the central value with strong positive upswings collocated with enhancements in TEC. The polarity changes in SuperDARN LOS velocities become more evident in Figure 8 which is in the same format as Figure 7 but for beam 18 of the FHW radar, which is the poleward looking beam near mid-western United States (see Figure 2). (TEC coverage is sparse in the region which produces the data gaps in panel (a) of Figure 8.) The main feature that stands out from the figure is the systematic polarity change in LOS velocities as the MSTIDs pass through the beam. The color bar

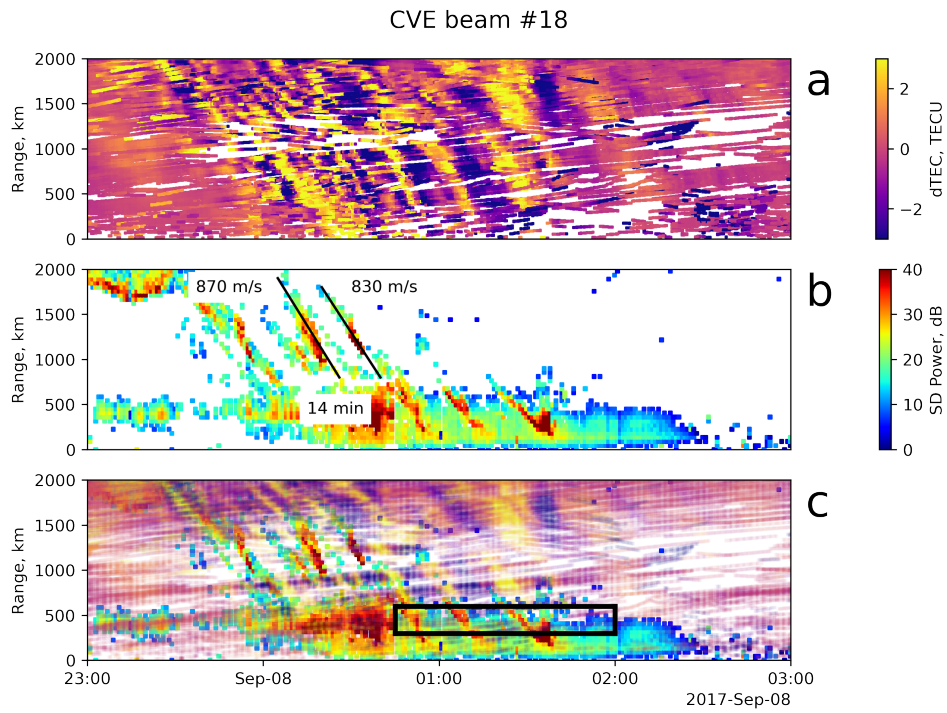


Figure 5. Comparison between SuperDARN and GNSS TEC measurements. Panel (a): de-trended GNSS TEC observations projected along CVE beam 18. Panel (b): CVE beam 18 measurements of backscatter power. Slope values allow for calculation of LOS phase speed. Panel (c) shows de-trended GNSS TEC from panel (a) and SuperDARN backscatter power from panel (b) overlaid on top of each other. The black boxed region contains data compared in 6.

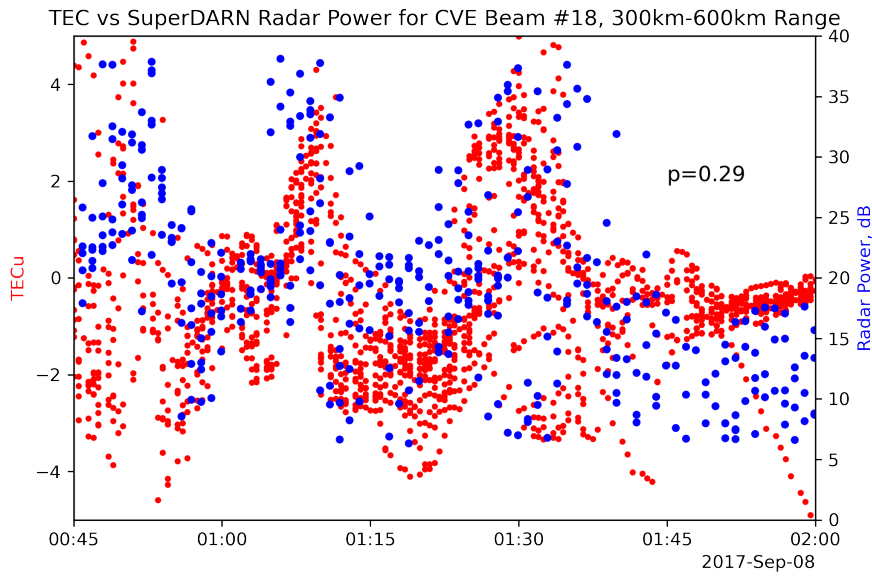


Figure 6. Time series plot showing correlation between maximum SuperDARN power level and mean detrended TEC. Data is taken between 300 and 600km along CVE Beam 18 shown in panel (c) of Figure 5. Rolling averages of the datasets are compared using a 1D Pearson correlation coefficient, resulting in $p=0.29$.

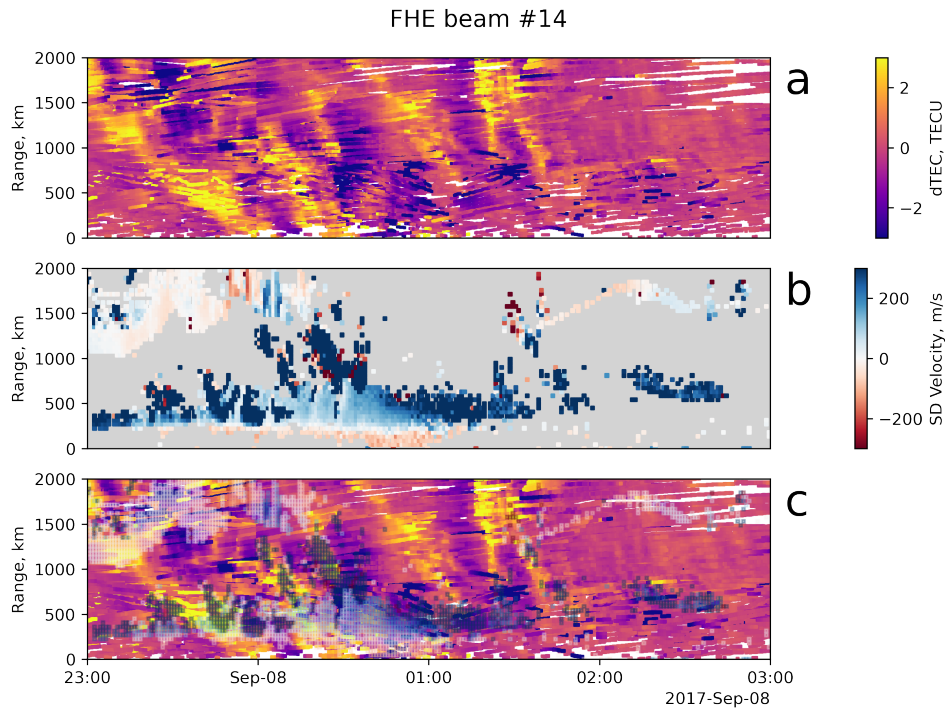


Figure 7. Comparison between SuperDARN LOS velocities and GNSS TEC measurements. Panel (a): de-trended GNSS TEC observations projected along FHE beam 14. Panel (b): FHE beam 14 measurements of LOS velocities. Panel (c) shows de-trended GNSS TEC from panel (a) and SuperDARN LOS velocities from panel (b) overlaid on top of each other.

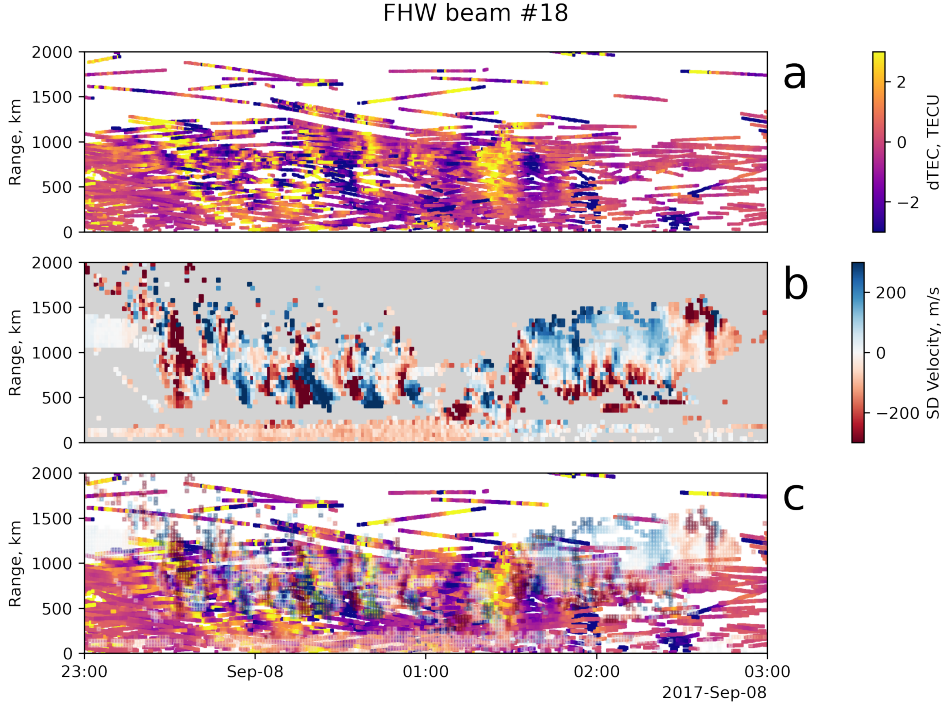


Figure 8. Same format as Figure 7 but for Fort Hays West Beam 18.

303 is now centered at 0, and velocities now oscillate with peak amplitudes exceeding ± 300
 304 m/s.

305 **4 Discussion**

306 In the previous sections, the characteristics of storm-time MSTIDs observed in high-
 307 resolution GNSS TEC and SuperDARN datasets were examined. Here, the current ob-
 308 servations will be compared with those presented in previous studies, and the role of dif-
 309 ferent factors in driving these storm-time MSTIDs will be determined.

310 An important feature from Figure 5 is that MSTID signatures in SuperDARN were
 311 observed in the near ranges (< 500 km) as well as the farther ranges (~ 1000 - 1500 km).
 312 Due to the nature of HF propagation, widely distributed backscatter from farther ranges
 313 is primarily due to F region irregularities, while backscatter from closer than about 600
 314 km must be due to E region irregularities (Chisham et al., 2008). The transition in backscat-
 315 ter mode can be appreciated in Figure 5 through the change in backscatter characteristics
 316 that occurs at about 600 km. Here the intermittent backscatter at further ranges gives
 317 way to continuous backscatter over the E region ranges. While SuperDARN slant range
 318 can provide some additional context regarding the region of the ionosphere producing
 319 the backscatter, it is difficult to resolve altitude profiles of electron density using the GNSS
 320 TEC dataset. However, it is likely that a significant contribution to the variability ob-
 321 served in TEC is coming from the F region, where electron densities are expected to be
 322 the highest, even during geomagnetic storms (Hocke et al., 2019). A comparison between
 323 Figures 2 and 5 shows that the variability in TEC (indicated by dTEC) was very strong
 324 ($\sim 50\%$ of the background values), suggesting that the F-region electron densities might
 325 be making significant contributions to the variability observed during this event. Over-
 326 all, these observations from SuperDARN and GNSS TEC suggest that there was a strong
 327 coupling between the E and the F regions of the ionosphere during this event such that

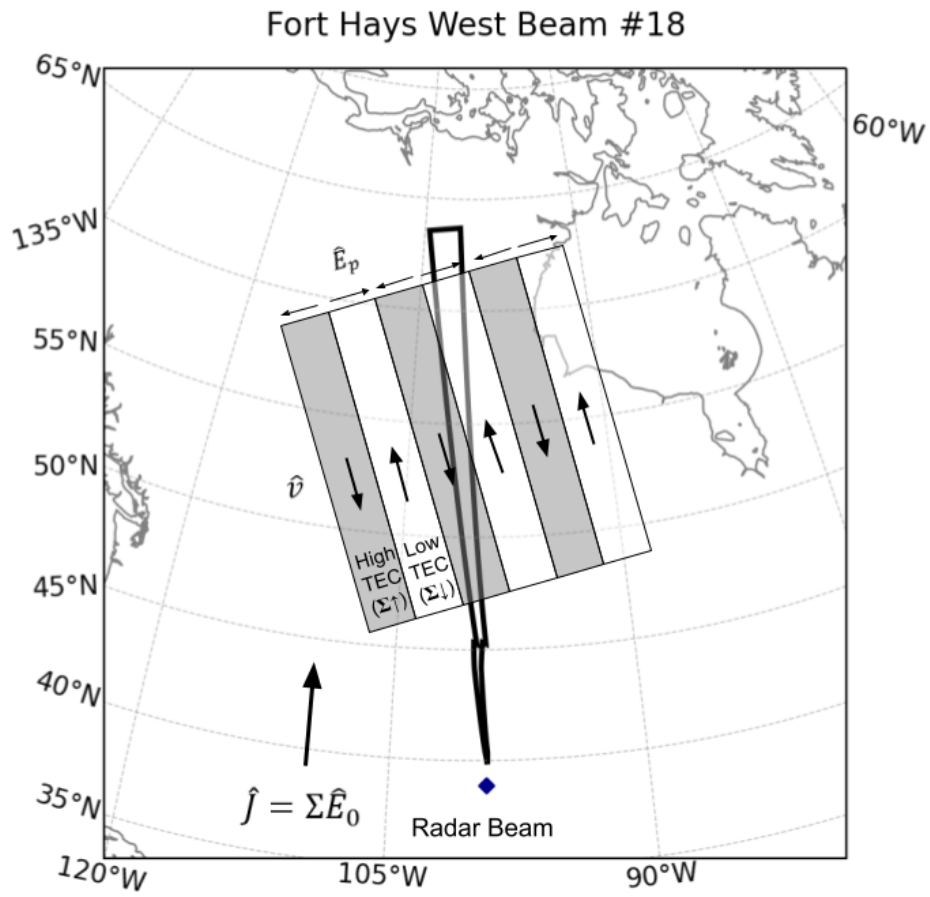


Figure 9. A schematic illustrating the proposed mechanism to explain the generation of polarization electric fields and their relation to MSTID wavefronts and background plasma convection. Polarization electric fields (E_P) are shown, as well as the resulting ExB drifts (\hat{v}).

328 MSTID signatures are observed in both regions. This raises a key question: Do these MSTIDs
 329 originate in the E-region or the F-region? It is possible that Hall current driven processes
 330 generate polarization electric fields in the E-region which map into the F region and drive
 331 MSTIDs (Tsunoda & Cosgrove, 2001). It is also possible that E region echoes in Super-
 332 DARN are modulated by MSTIDs originating in the F-region. Previous studies have sug-
 333 gested that coupling between the E- and the F-regions and sporadic-E layers can aug-
 334 ment and enhance the instabilities associated with MSTIDs (Otsuka et al., 2007; Ogawa
 335 et al., 2009). The Gradient Drift Instability (GDI) was suggested to be the primary plasma
 336 instability mechanism generating field-aligned irregularities observed by SuperDARN in
 337 such a case (Hiyadutuje et al., 2022). Regardless of the source region, it is clear that inter-
 338 region electrodynamics across altitude likely play a key role in furthering the plasma in-
 339 stability driving these storm time MSTIDs.

340 From Figure 1, it can be noted that the MSTIDs reported during this event were
 341 observed during the initial phases of a major geomagnetic storm. S. R. Zhang et al. (2019)
 342 analyzed the same event using the high-resolution GNSS TEC dataset and suggested two
 343 possibilities. The first is that ion-neutral frictional heating from the westward SAPS flows
 344 in the region produces AGWs and associated MSTIDs. Global Ionosphere-Thermosphere
 345 model (GITM) simulations presented by Guo et al. (2018) showed that strong SAPS flows
 346 can significantly heat the thermosphere and drive TIDs. The second possibility is that
 347 polarization electric fields induced by an electrodynamic instability (e.g., Perkins, 1973)
 348 are driving the MSTIDs. It is not possible to determine if electrodynamic instabilities
 349 are driving the MSTIDs based solely on GNSS TEC data. Instead, additional measure-
 350 ments, such as those showing polarization electric fields, are needed. A few previous stud-
 351 ies have shown that polarization electric fields, which systematically switch polarities be-
 352 tween the crests and troughs in MSTIDs, manifest as oscillations in SuperDARN Doppler
 353 velocities (e.g., Ogawa et al., 2009; Suzuki et al., 2009). Such oscillations in the line-of-
 354 sight Doppler velocities are clearly evident during the current event, in beam 14 of the
 355 FHE (Figure 7) and beam 18 of the FHW (Figure 8) radars. The SuperDARN obser-
 356 vations therefore confirm the presence of polarization electric fields during this event, and
 357 are in agreement with the conjecture made by S. R. Zhang et al. (2019) that these MSTIDs
 358 are driven by an electrodynamic instability. Finally, the south-westward propagation of
 359 MSTIDs observed during this event is similar to observations of electrified MSTIDs re-
 360 ported previously by Ogawa et al. (2009), which has been attributed to preferential Joule
 361 damping associated with electrodynamic instability processes (Kelley, 2011).

362 Previous studies have used mid-latitude SuperDARN observations in the Japanese
 363 sector to identify and analyze electrified MSTIDs driven by polarization electric fields
 364 (Ogawa et al., 2009; Suzuki et al., 2009). However, these reports focused on geomagnet-
 365 ically quiet intervals. Consequently, the main differentiating factor between the current
 366 observations and previous reports is the strong geomagnetic driving during this event
 367 (see Figure 1). We note from Figures 5, 7, and 8 that both the radar power and LOS
 368 velocity amplitude variations are almost an order of magnitude stronger than those re-
 369 ported previously. These differences are perhaps unsurprising, as this study is of an in-
 370 tense storm time event, and the mid-latitude electrodynamics are expected to be dom-
 371 inated by strong SAPS electric fields (S. R. Zhang et al., 2019). During geomagnetically
 372 quiet intervals, the mid-latitude electric fields are expected to be relatively weaker and
 373 driven by neutral winds (Suzuki et al., 2009). An examination of Figure 4 shows that
 374 the background plasma convection is predominantly westwards during the MSTIDs. The
 375 spatio-temporal relationship between SuperDARN LOS velocity and TEC enhancements/depletions
 376 observed during the current event is different when compared to previous reports of quiet-
 377 time electrified MSTIDs (Otsuka et al., 2007, 2009; Suzuki et al., 2009). Specifically, en-
 378 hancements in SuperDARN power during this event are aligned with enhancements in
 379 GNSS TEC (Figures 5 and 6), in contrast to quiet-time events where strong HF echoes
 380 were correlated with depletions in airglow/TEC (Otsuka et al., 2007, 2009; Suzuki et al.,
 381 2009; Ogawa et al., 2009). An interpretation of these observations is presented in Fig-

382 ure 9. The figure shows MSTID wavefronts passing through a poleward-directed radar
 383 beam. Regions of high TEC (conductivity) are shaded in dark. The directions of induced
 384 polarization electric fields (E_P) and the corresponding ExB drifts (\hat{v}) are marked in the
 385 figure. In the F-region, at mid-latitudes, the Pedersen current can be given as $J_P = \Sigma_p(E_0 +$
 386 $U \times B)$, here E_0 is the background electric field, U is the neutral wind velocity, and B
 387 is the magnetic field. The westward directed plasma convection observed during the event,
 388 likely associated with SAPS, suggests that E_0 is the dominant component and is pre-
 389 dominantly northwards. U is assumed to be much smaller compared to E_0 since the event
 390 was observed during the early phases of a storm and the role of the neutral wind (the
 391 disturbance dynamo) is expected to be significant during the recovery phase (Blanc &
 392 Richmond, 1980). Consequently, J_P is also directed northwards, in the same direction
 393 as E_0 . Note that the electrodynamics during the event are significantly different from
 394 the quiet-time events ($K_p = 0$) reported by Suzuki et al. (2009) which assume U is the
 395 dominant component and neglect the role of E_0 . To maintain current continuity, polar-
 396 ization electric fields are induced orthogonal to the MSTID wave fronts by J_P such that
 397 they are directed north-eastwards(south-westwards) in regions of TEC depletion(enhancement).
 398 In other words, the polarization electric field has a component in the direction of J_P in
 399 regions of reduced conductivity, and away in regions of enhanced conductivity. The scen-
 400 ario is illustrated in Figure 9. The ExB drift associated with these polarization elec-
 401 tric fields would be directed towards (positive LOS velocities) the radar in regions with
 402 high TEC, and away (negative LOS velocities) in regions with low TEC. Since the ExB
 403 drifts associated with the polarization electric fields are expected to be predominantly
 404 meridional, the corresponding velocity changes will be prominent in poleward-directed
 405 beams, such as beam 18 of FHW (Figure 8). This mechanism is consistent with the sense
 406 of the observations presented in Figures 7 and 8. For example, Figure 7.b two distinct
 407 MSTID wave fronts are observed between midnight and 1:00 UT as enhancements in TEC,
 408 and corresponding SuperDARN observations show positive (blue/towards the radar) LOS
 409 velocities collocated with these enhancements.

410 Overall, this study presents a new class of electrified MSTIDs that are distinct from
 411 the typical quiet-time MSTIDs reported previously (Otsuka et al., 2004, 2007; Ogawa
 412 et al., 2009, e.g.). The oscillations in SuperDARN LOS velocities and dTEC were al-
 413 most an order of magnitude stronger than those observed during quiet-times (Suzuki et
 414 al., 2009) and a new mechanism has been proposed to explain the generation of polar-
 415 ization electric fields during intervals of strong geomagnetic driving.

416 5 Conclusions

417 This study has analyzed observations of MSTIDs during the September 7th/8th
 418 2017 geomagnetic storm event, over mid-latitude North America. The event interval was
 419 characterized by strong geomagnetic driving with K_p reaching 9, and $SymH$ dropping
 420 to nearly -200 nT. Signatures of MSTIDs were observed in both GNSS TEC and iono-
 421 spheric backscatter in SuperDARN, with similar time-periods (~ 15 minutes), wavelength
 422 (~ 700 km), and phase speeds (~ 600 m/s). In SuperDARN, the MSTIDs produced os-
 423 cillations ranging ± 500 m/s in LOS velocities, and in detrended GNSS TEC strong per-
 424 turbations reaching up to 50% of the background TEC value were observed. These MSTIDs
 425 were propagating in the southwestward direction, similar to previous reports of MSTIDs
 426 observed on the nightside. SuperDARN data showed that the MSTID signatures were
 427 observed in both near and farther ranges, suggesting strong coupling between the E and
 428 the F-regions. Projecting detrended GNSS TEC data along SuperDARN beams showed
 429 that enhancements in TEC were positively correlated with increases in SuperDARN SNR,
 430 contrary to previous observations which showed that these parameters were anti-correlated,
 431 at least in quiet time events. Strong oscillations in LOS velocities observed in SuperDARN
 432 indicated a systematic reversal in the polarity of the electric fields between the crests and
 433 troughs of the MSTIDs, confirming the presence of polarization electric fields during the

434 event. The poleward directed background electric fields associated with westward directed
 435 plasma convection observed during the event were hypothesized to generate the polar-
 436 ization electric fields. Overall, the storm-time MSTIDs reported in this study were driven
 437 by an electrodynamic instability and were distinct from previous reports of electrified
 438 MSTIDs which were observed during quiet geomagnetic intervals.

439 6 Open Research

440 SuperDARN data can be found at the Virginia Tech SuperDARN webpage at [https://](https://www.frdr-dfdr.ca/repo/collection/superdarn)
 441 www.frdr-dfdr.ca/repo/collection/superdarn. SuperDARN data has been processed
 442 using the Radar Software Toolkit (Burrell et al., 2022). LOS GNSS TEC data is avail-
 443 able at <http://www.openmadrigal.org>. Individual GNSS TEC data files used in this
 444 study can be found at [https://w3id.org/cedar?experiment_list=experiments2/2017/](https://w3id.org/cedar?experiment_list=experiments2/2017/gps/07sep17&file_list=los_20170907.004.h5)
 445 [gps/07sep17&file_list=los_20170907.004.h5](https://w3id.org/cedar?experiment_list=experiments2/2017/gps/07sep17&file_list=los_20170907.004.h5) and [https://w3id.org/cedar?experiment](https://w3id.org/cedar?experiment_list=experiments2/2017/gps/08sep17&file_list=los_20170908.004.h5)
 446 [_list=experiments2/2017/gps/08sep17&file_list=los_20170908.004.h5](https://w3id.org/cedar?experiment_list=experiments2/2017/gps/08sep17&file_list=los_20170908.004.h5). Data pro-
 447 cessing and visualization was done using open-source software, including Matplotlib (Hunter,
 448 2007), Pandas (Wes McKinney, 2010), IPython (Pérez & Granger, 2007), Cartopy (Met
 449 Office, 2010 - 2013), Scipy (Virtanen et al., 2020), and others (Millman & Aivazis, 2011).

450 Acknowledgments

451 The authors thank the National Science Foundation for support by grants AGS-1935110,
 452 and AGS-1952737. BSRK and JBHB acknowledge National Science Foundation for sup-
 453 port by grants AGS-1822056, and AGS-1839509. The Christmas Valley SuperDARN radars
 454 are maintained and operated by Dartmouth College under support by NSF grant AGS-
 455 1934997. SuperDARN is a worldwide collection of radars funded by various national fund-
 456 ing agencies of Australia, Canada, China, France, Italy, Japan, Norway, South Africa,
 457 United Kingdom, and the United States of America. SuperDARN data used in this study
 458 can be accessed from the following website: [https://www.frdr-dfdr.ca/repo/collection/](https://www.frdr-dfdr.ca/repo/collection/superdarn)
 459 [superdarn](https://www.frdr-dfdr.ca/repo/collection/superdarn). The geomagnetic indices used in this paper can be obtained from NASA's
 460 OMNIWeb service (<https://omniweb.gsfc.nasa.gov/form/dx1.html>). GPS TEC data prod-
 461 ucts and access through the Madrigal distributed data system are provided to the com-
 462 munity by the Massachusetts Institute of Technology under support from US National
 463 Science Foundation grant AGS-1952737. Data for the TEC processing is provided from
 464 the following organizations: UNAVCO, Scripps Orbit and Permanent Array Center, In-
 465 stitut Geographique National, France, International GNSS Service, The Crustal Dynam-
 466 ics Data Information System (CDDIS), National Geodetic Survey, Instituto Brasileiro
 467 de Geografia e Estatística, RAMSAC CORS of Instituto Geográfico Nacional de la República
 468 Argentina, Arecibo Observatory, Low-Latitude Ionospheric Sensor Network (LISN), Top-
 469 con Positioning Systems, Inc., Canadian High Arctic Ionospheric Network, Institute of
 470 Geology and Geophysics, Chinese Academy of Sciences, China Meteorology Administra-
 471 tion, Centro di Ricerche Sismologiche, Système d'Observation du Niveau des Eaux Lit-
 472 torales (SONEL), RENAG : REseau NAtional GPS permanent, GeoNet - the official source
 473 of geological hazard information for New Zealand, GNSS Reference Networks, Finnish
 474 Meteorological Institute, SWEPOS - Sweden, Hartebeesthoek Radio Astronomy Obser-
 475 vatory, TrigNet Web Application, South Africa, Australian Space Weather Services, RETE
 476 INTEGRATA NAZIONALE GPS, Estonian Land Board, Virginia Tech Center for Space
 477 Science and Engineering Research, and Korea Astronomy and Space Science Institute.

478 References

- 479 André, D., Sofko, G. J., Baker, K., & MacDougall, J. (1998, 4). Superdarn interfer-
 480 ometry: Meteor echoes and electron densities from groundscatter. *Journal of Geo-*
 481 *physical Research: Space Physics*, *103*, 7003-7015. doi: 10.1029/97JA02923
 482 Baker, J. B., Greenwald, R. A., Ruohoniemi, J. M., Oksavik, K., Gjerloev, J. W.,

- 483 Paxton, L. J., & Hairston, M. R. (2007, 1). Observations of ionospheric convection
 484 from the wallops superdarn radar at middle latitudes. *Journal of Geophysical*
 485 *Research: Space Physics*, *112*, 1303. doi: 10.1029/2006JA011982
- 486 Blanc, M., & Richmond, A. (1980). The ionospheric disturbance dynamo. *Journal*
 487 *of Geophysical Research: Space Physics*, *85*(A4), 1669-1686. doi: [https://doi.org/](https://doi.org/10.1029/JA085iA04p01669)
 488 [10.1029/JA085iA04p01669](https://doi.org/10.1029/JA085iA04p01669)
- 489 Borries, C., Jakowski, N., & Wilken, V. (2009). Storm induced large scale tids ob-
 490 served in gps derived tec. *Annales Geophysicae*, *27*, 1605-1612. doi: 10.5194/
 491 ANGE0-27-1605-2009
- 492 Bristow, W. A., Greenwald, R. A., & Samson, J. C. (1994, 1). Identification of
 493 high-latitude acoustic gravity wave sources using the goose bay hf radar. *Journal*
 494 *of Geophysical Research: Space Physics*, *99*, 319-331. doi: 10.1029/93JA01470
- 495 Burrell, A., Thomas, E., Schmidt, M., Bland, E., Coco, I., Ponomarenko, P., ...
 496 Walach, M.-T. (2022, April). *Superdarn/rst: Rst 4.7*. Zenodo. Retrieved from
 497 <https://doi.org/10.5281/zenodo.6473603> doi: 10.5281/zenodo.6473603
- 498 Chimonas, G., & Hines, C. O. (1970, 4). Atmospheric gravity waves launched by
 499 auroral currents. *Planetary and Space Science*, *18*, 565-582. doi: 10.1016/0032-
 500 -0633(70)90132-7
- 501 Chisham, G., Lester, A. M., Milan, A. S. E., Freeman, A. M. P., Bristow, A. W. A.,
 502 Grocott, A. A., ... Sato, N. (2007, 5). A decade of the super dual au-
 503 roral radar network (superdarn): scientific achievements, new techniques
 504 and future directions. *Surveys in Geophysics 2007 28:1*, *28*, 33-109. doi:
 505 [10.1007/S10712-007-9017-8](https://doi.org/10.1007/S10712-007-9017-8)
- 506 Chisham, G., Yeoman, T. K., & Sofko, G. J. (2008). Mapping ionospheric
 507 backscatter measured by the superdarn hf radars – part 1: A new empiri-
 508 cal virtual height model. *Annales Geophysicae*, *26*(4), 823–841. Retrieved
 509 from <https://angeo.copernicus.org/articles/26/823/2008/> doi:
 510 [10.5194/angeo-26-823-2008](https://doi.org/10.5194/angeo-26-823-2008)
- 511 Chou, M. Y., Lin, C. C., Yue, J., Tsai, H. F., Sun, Y. Y., Liu, J. Y., & Chen,
 512 C. H. (2017, 2). Concentric traveling ionosphere disturbances triggered by su-
 513 per typhoon meranti (2016). *Geophysical Research Letters*, *44*, 1219-1226. doi:
 514 [10.1002/2016GL072205](https://doi.org/10.1002/2016GL072205)
- 515 Davis, T. N., & Sugiura, M. (1966). Auroral electrojet activity index ae and its uni-
 516 versal time variations. *Journal of Geophysical Research (1896-1977)*, *71*(3), 785-
 517 801. doi: <https://doi.org/10.1029/JZ071i003p00785>
- 518 Ding, F., Wan, W., Ning, B., & Wang, M. (2007, 6). Large-scale traveling iono-
 519 spheric disturbances observed by gps total electron content during the magnetic
 520 storm of 29–30 october 2003. *Journal of Geophysical Research: Space Physics*,
 521 *112*, 6309. doi: 10.1029/2006JA012013
- 522 Duly, T. M., Chapagain, N. P., & Makela, J. J. (2013, 12). Climatology of night-
 523 time medium-scale traveling ionospheric disturbances (mstids) in the central
 524 pacific and south american sectors. *Annales Geophysicae*, *31*, 2229-2237. doi:
 525 [10.5194/ANGE0-31-2229-2013](https://doi.org/10.5194/ANGE0-31-2229-2013)
- 526 Frissell, N. A., Baker, J. B., Ruohoniemi, J. M., Gerrard, A. J., Miller, E. S.,
 527 Marini, J. P., ... Bristow, W. A. (2014). Climatology of medium-scale travel-
 528 ing ionospheric disturbances observed by the midlatitude blackstone superdarn
 529 radar. *Journal of Geophysical Research: Space Physics*, *119*, 7679-7697. doi:
 530 [10.1002/2014JA019870](https://doi.org/10.1002/2014JA019870)
- 531 Fukao, S., Kelley, M. C., Shirakawa, T., Takami, T., Yamamoto, M., Tsuda, T., &
 532 Kato, S. (1991, 3). Turbulent upwelling of the mid-latitude ionosphere: 1. obser-
 533 vational results by the mu radar. *Journal of Geophysical Research: Space Physics*,
 534 *96*, 3725-3746. doi: 10.1029/90JA02253
- 535 Garcia, F. J., Kelley, M. C., Makela, J. J., & Huang, C. S. (2000, 8). Airglow
 536 observations of mesoscale low-velocity traveling ionospheric disturbances at mid-

- latitudes. *Journal of Geophysical Research: Space Physics*, *105*, 18407-18415. doi: 10.1029/1999JA000305
- Georges, T. M. (1968, 1). Hf doppler studies of traveling ionospheric disturbances. *Journal of Atmospheric and Terrestrial Physics*, *30*, 735-746. doi: 10.1016/S0021-9169(68)80029-7
- Greenwald, R. A., Baker, K. B., Dudeney, J. R., Pinnock, M., Jones, T. B., Thomas, E. C., ... Yamagishi, H. (1995, 2). Darn/superdarn. *Space Science Reviews* *1995* *71:1*, *71*, 761-796. doi: 10.1007/BF00751350
- Grocott, A., Hosokawa, K., Ishida, T., Lester, M., Milan, S. E., Freeman, M. P., ... Yukimatu, A. S. (2013, 9). Characteristics of medium-scale traveling ionospheric disturbances observed near the antarctic peninsula by hf radar. *Journal of Geophysical Research: Space Physics*, *118*, 5830-5841. doi: 10.1002/JGRA.50515
- Guo, J., Deng, Y., Zhang, D., Lu, Y., Sheng, C., & Zhang, S. (2018, 3). The effect of subauroral polarization streams on ionosphere and thermosphere during the 2015 st. patrick's day storm: Global ionosphere-thermosphere model simulations. *Journal of Geophysical Research: Space Physics*, *123*, 2241-2256. doi: 10.1002/2017JA024781
- Hines, C. O. (1960, 11). Internal atmospheric gravity waves at ionospheric heights. *Canadian Journal of Physics*, *38*, 1441-1481. doi: 10.1139/P60-150
- Hiyadutuje, A., Kosch, M. J., & Stephenson, J. A. E. (2022, 5). First observations of e-region near range echoes partially modulated by f-region traveling ionospheric disturbances observed by the same superdarn hf radar. *Journal of Geophysical Research: Space Physics*, *127*, e2021JA030157. doi: 10.1029/2021JA030157
- Hocke, K., Liu, H., Pedatella, N., & Ma, G. (2019, 4). Global sounding of f region irregularities by cosmic during a geomagnetic storm. *Annales Geophysicae*, *37*, 235-242. doi: 10.5194/ANGE0-37-235-2019
- Hocke, K., & Schlegel, K. (1996, 9). A review of atmospheric gravity waves and travelling ionospheric disturbances: 1982-1995. *Annales Geophysicae*, *14*, 917-940. doi: 10.1007/S00585-996-0917-6
- Huang, F., Dou, X., Lei, J., Lin, J., Ding, F., & Zhong, J. (2016, 9). Statistical analysis of nighttime medium-scale traveling ionospheric disturbances using airglow images and gps observations over central china. *Journal of Geophysical Research: Space Physics*, *121*, 8887-8899. doi: 10.1002/2016JA022760
- Hunsucker, R. D. (1982, 5). Atmospheric gravity waves generated in the high-latitude ionosphere: A review. *Reviews of Geophysics*, *20*, 293-315. doi: 10.1029/RG020I002P00293
- Hunter, J. D. (2007). Matplotlib: A 2d graphics environment. *Computing In Science & Engineering*, *9*(3), 90-95. doi: 10.1109/MCSE.2007.55
- Iyemori, T. (1990). Storm-time magnetospheric currents inferred from mid-latitude geomagnetic field variations. *Journal of geomagnetism and geoelectricity*, *42*, 1249-1265. doi: 10.5636/jgg.42.1249
- Kelley, M. C. (2011). On the origin of mesoscale tids at midlatitudes. *Annales Geophysicae*, *29*, 361-366. doi: 10.5194/ANGE0-29-361-2011
- King, J. H., & Papitashvili, N. E. (2005, 2). Solar wind spatial scales in and comparisons of hourly wind and ace plasma and magnetic field data. *Journal of Geophysical Research*, *110*, A02104. doi: 10.1029/2004JA010649
- Kunduri, B. S. R., Baker, J. B. H., Ruohoniemi, J. M., Nishitani, N., Oksavik, K., Erickson, P. J., ... Miller, E. S. (2018). A new empirical model of the subauroral polarization stream. *Journal of Geophysical Research: Space Physics*, *123*(9), 7342-7357. doi: https://doi.org/10.1029/2018JA025690
- Liu, J.-Y., Chen, C.-H., Lin, C.-H., Tsai, H.-F., Chen, C.-H., Kamogawa, M., ... Kamogawa, M. (2011, 6). Ionospheric disturbances triggered by the 11 march 2011 m9.0 tohoku earthquake. *Journal of Geophysical Research: Space Physics*, *116*, 6319. doi: 10.1029/2011JA016761

- 591 Lyons, L. R., Nishimura, Y., Zhang, S. R., Coster, A. J., Bhatt, A., Kendall, E., &
592 Deng, Y. (2019, 1). Identification of auroral zone activity driving large-scale trav-
593 eling ionospheric disturbances. *Journal of Geophysical Research: Space Physics*,
594 *124*, 700-714. doi: 10.1029/2018JA025980
- 595 Met Office. (2010 - 2013). Cartopy: a cartographic python library with matplotlib
596 support [Computer software manual]. Exeter, Devon. Retrieved from [https://](https://scitools.org.uk/cartopy)
597 scitools.org.uk/cartopy
- 598 Miller, C. A. (1997, 6). Electrodynamics of midlatitude spread f 2. a new theory of
599 gravity wave electric fields. *Journal of Geophysical Research: Space Physics*, *102*,
600 11533-11538. doi: 10.1029/96JA03840
- 601 Millman, K. J., & Aivazis, M. (2011, March-April). Python for scientists and en-
602 gineers. *Computing in Science & Engineering*, *13*(2), 9-12. doi: 10.1109/MCSE
603 .2011.36
- 604 Munro, G. H. (1948). Short-period changes in the f region of the ionosphere. *Nature*
605 *1948 162:4127, 162*, 886-887. doi: 10.1038/162886a0
- 606 Nishitani, N., Ruohoniemi, J. M., Lester, M., Baker, J. B. H., Koustov, A. V., Shep-
607 herd, S. G., ... Kikuchi, T. (2019, 3). Review of the accomplishments of mid-
608 latitude super dual auroral radar network (superdarn) hf radars. *Progress in Earth*
609 *and Planetary Science 2019 6:1, 6*, 1-57. doi: 10.1186/S40645-019-0270-5
- 610 Ogawa, T., Nishitani, N., Otsuka, Y., Shiokawa, K., Tsugawa, T., & Hosokawa, K.
611 (2009, 3). Medium-scale traveling ionospheric disturbances observed with the
612 superdarn hokkaido radar, all-sky imager, and gps network and their relation
613 to concurrent sporadic e irregularities. *Journal of Geophysical Research: Space*
614 *Physics*, *114*, 3316. doi: 10.1029/2008JA013893
- 615 Otsuka, Y., Onoma, F., Shiokawa, K., Ogawa, T., Yamamoto, M., & Fukao,
616 S. (2007, 6). Simultaneous observations of nighttime medium-scale travel-
617 ing ionospheric disturbances and e region field-aligned irregularities at mid-
618 latitude. *Journal of Geophysical Research: Space Physics*, *112*, 6317. doi:
619 10.1029/2005JA011548
- 620 Otsuka, Y., Shiokawa, K., Ogawa, T., & Wilkinson, P. (2004, 8). Geomagnetic
621 conjugate observations of medium-scale traveling ionospheric disturbances at mid-
622 latitude using all-sky airglow imagers. *Geophysical Research Letters*, *31*. doi:
623 10.1029/2004GL020262
- 624 Otsuka, Y., Shiokawa, K., Ogawa, T., Yokoyama, T., & Yamamoto, M. (2009, 5).
625 Spatial relationship of nighttime medium-scale traveling ionospheric disturbances
626 and f region field-aligned irregularities observed with two spaced all-sky airglow
627 imagers and the middle and upper atmosphere radar. *Journal of Geophysical*
628 *Research: Space Physics*, *114*. doi: 10.1029/2008JA013902
- 629 Pérez, F., & Granger, B. E. (2007, May). IPython: a system for interactive scientific
630 computing. *Computing in Science and Engineering*, *9*(3), 21-29. Retrieved from
631 <http://ipython.org> doi: 10.1109/MCSE.2007.53
- 632 Perkins, F. (1973, 1). Spread f and ionospheric currents. *Journal of Geophysical Re-*
633 *search*, *78*, 218-226. doi: 10.1029/JA078I001P00218
- 634 Rideout, W., & Coster, A. (2006, 7). Automated gps processing for global total elec-
635 tron content data. *GPS Solutions*, *10*, 219-228.
- 636 Ruohoniemi, J. M., Greenwald, R. A., Baker, K. B., Villain, J. P., & Mc-
637 Cready, M. A. (1987, 5). Drift motions of small-scale irregularities in the
638 high-latitude f region: An experimental comparison with plasma drift mo-
639 tions. *Journal of Geophysical Research: Space Physics*, *92*, 4553-4564. doi:
640 10.1029/JA092IA05P04553
- 641 Saito, A., Fukao, S., & Miyazaki, S. (1998, 8). High resolution mapping of tec per-
642 turbations with the gsi gps network over japan. *Geophysical Research Letters*, *25*,
643 3079-3082. doi: 10.1029/98GL52361
- 644 Samson, J. C., Greenwald, R. A., Ruohoniemi, J. M., Frey, A., & Baker, K. B.

- (1990, 6). Goose bay radar observations of earth-reflected, atmospheric gravity waves in the high-latitude ionosphere. *Journal of Geophysical Research: Space Physics*, *95*, 7693-7709. doi: 10.1029/JA095IA06P07693
- Shiokawa, K., Otsuka, Y., Ihara, C., Ogawa, T., & Rich, F. J. (2003, 4). Ground and satellite observations of nighttime medium-scale traveling ionospheric disturbance at midlatitude. *Journal of Geophysical Research: Space Physics*, *108*. doi: 10.1029/2002JA009639
- Suzuki, S., Hosokawa, K., Otsuka, Y., Shiokawa, K., Ogawa, T., Nishitani, N., . . . Shevtsov, B. M. (2009, 7). Coordinated observations of nighttime medium-scale traveling ionospheric disturbances in 630-nm airglow and hf radar echoes at midlatitudes. *Journal of Geophysical Research: Space Physics*, *114*, 7312. doi: 10.1029/2008JA013963
- Tsugawa, T., Otsuka, Y., Coster, A. J., & Saito, A. (2007, 11). Medium-scale traveling ionospheric disturbances detected with dense and wide tec maps over north america. *Geophysical Research Letters*, *34*, 22101. doi: 10.1029/2007GL031663
- Tsunoda, R. T., & Cosgrove, R. B. (2001, 11). Coupled electrodynamic in the nighttime midlatitude ionosphere. *Geophysical Research Letters*, *28*, 4171-4174. doi: 10.1029/2001GL013245
- Vadas, S. L. (2007, 6). Horizontal and vertical propagation and dissipation of gravity waves in the thermosphere from lower atmospheric and thermospheric sources. *Journal of Geophysical Research: Space Physics*, *112*, n/a-n/a. doi: 10.1029/2006JA011845
- Valladares, C. E., & Sheehan, R. (2016, 9). Observations of conjugate mstids using networks of gps receivers in the american sector. *Radio Science*, *51*, 1470-1488. doi: 10.1002/2016RS005967
- Vierinen, J., Coster, A. J., Rideout, W. C., Erickson, P. J., & Norberg, J. (2016, 3). Statistical framework for estimating gnss bias. *Atmospheric Measurement Techniques*, *9*, 1303-1312. doi: 10.5194/AMT-9-1303-2016
- Virtanen, P., Gommers, R., Oliphant, T. E., Haberland, M., Reddy, T., Cournapeau, D., . . . SciPy 1.0 Contributors (2020). SciPy 1.0: Fundamental Algorithms for Scientific Computing in Python. *Nature Methods*, *17*, 261-272. doi: 10.1038/s41592-019-0686-2
- Wes McKinney. (2010). Data Structures for Statistical Computing in Python. In Stéfan van der Walt & Jarrod Millman (Eds.), *Proceedings of the 9th Python in Science Conference* (p. 56 - 61). doi: 10.25080/Majora-92bf1922-00a
- Zhang, S., Erickson, P. J., Zhang, Y., Wang, W., Huang, C., Coster, A. J., . . . Kerr, R. (2017, 1). Observations of ion-neutral coupling associated with strong electrodynamic disturbances during the 2015 st. patrick's day storm. *Journal of Geophysical Research: Space Physics*, *122*, 1314-1337. doi: 10.1002/2016JA023307
- Zhang, S. R., Erickson, P. J., Coster, A. J., Rideout, W., Vierinen, J., Jonah, O., & Goncharenko, L. P. (2019, 12). Subauroral and polar traveling ionospheric disturbances during the 7-9 september 2017 storms. *Space Weather*, *17*, 1748-1764. doi: 10.1029/2019SW002325
- Zhang, S. R., Erickson, P. J., Goncharenko, L. P., Coster, A. J., Rideout, W., & Vierinen, J. (2017, 12). Ionospheric bow waves and perturbations induced by the 21 august 2017 solar eclipse. *Geophysical Research Letters*, *44*, 12,067-12,073. doi: 10.1002/2017GL076054